Stiffness of targeted layer-by-layer nanoparticles impacts elimination half-life, tumor accumulation, and tumor penetration

Stephanie M. Kong[a,b], **Daniel F. Costa**[a], **Anna Jagielska**[c], **Krystyn J. Van Vliet**[c,d], and **Paula T. Hammond**[a,b,1]

[a]Koch Institute for Integrative Cancer Research, Massachusetts Institute of Technology, Cambridge, MA 02139; [b]Department of Chemical Engineering, Massachusetts Institute of Technology, Cambridge, MA 02139; [c]Department of Materials Science, Massachusetts Institute of Technology, Cambridge, MA 02139; and [d]Department of Biological Engineering, Massachusetts Institute of Technology, Cambridge, MA 02139

Edited by Joseph M. DeSimone, Stanford University, Stanford, CA, and approved August 9, 2021 (received for review March 11, 2021)

Nanoparticle (NP) stiffness has been shown to significantly impact circulation time and biodistribution in anticancer drug delivery. In particular, the relationship between particle stiffness and tumor accumulation and penetration in vivo is an important phenomenon to consider in optimizing NP-mediated tumor delivery. Layer-by-layer (LbL) NPs represent a promising class of multifunctional nanoscale drug delivery carriers. However, there has been no demonstration of the versatility of LbL systems in coating systems with different stiffnesses, and little is known about the potential role of LbL NP stiffness in modulating in vivo particle trafficking, although NP modulus has been recently studied for its impact on pharmacokinetics. LbL nanotechnology enables NPs to be functionalized with uniform coatings possessing molecular tumor-targeting properties, independent of the NP core stiffness. Here, we report that the stiffness of LbL NPs is directly influenced by the mechanical properties of its underlying liposomal core, enabling the modulation and optimization of LbL NP stiffness while preserving LbL NP outer layer tumor-targeting and stealth properties. We demonstrate that the stiffness of LbL NPs has a direct impact on NP pharmacokinetics, organ and tumor accumulation, and tumor penetration—with compliant LbL NPs having longer elimination half-life, higher tumor accumulation, and higher tumor penetration. Our findings underscore the importance of NP stiffness as a design parameter in enhancing the delivery of LbL NP formulations.

drug delivery | liposomes | targeting | modulus | cancer

For anticancer therapeutics that exhibit poor pharmacokinetic properties, dose-limiting toxicities, and chemical instability, nanoscale encapsulation and drug delivery offer a promising opportunity to confer favorable material properties that extend circulation half-life, control off-target tissue distribution, and limit the degradation or aggregation of unstable or poorly soluble therapeutic modalities. Layer-by-layer nanoparticles (LbL NPs), formed via the sequential, electrostatic assembly of oppositely charged polyelectrolytes on a colloidal template, enable the creation of multifunctional materials, whose properties can be tuned by switching out each charged component of the LbL NP system with a similarly charged polyelectrolyte. This modular platform allows for the facile integration of a wide variety of therapeutics (1–4) and functionalization with targeting chemistry that limits opsonization and clearance (5), while increasing tumor accumulation via receptor–ligand binding interactions and stimulus-responsive polymer architecture (6). LbL is a well-established technology with demonstrated applications in therapeutic targeting and systemic delivery to cancer (3, 7, 8).

Inspired by a number of studies chronicling the importance of mechanical properties on NP circulation half-life (9–13), tumor accumulation (14–16), and tumor penetration (17–21), and capitalizing on the adaptability of LbL NPs to be synthesized with a wide variety of charged core materials while maintaining the same tumor-targeting outer layer chemistry, we sought to determine whether LbL NPs preserve the stiffness properties of their cores, enabling LbL NP stiffness to be tuned for desired half-life and tumor accumulation and penetration, while simultaneously conserving tumor-targeting and stealth properties provided by the LbL particle coating. We examined whether core-imparted LbL NP stiffness could impact particle pharmacokinetics and tumor accumulation and penetration. Using an LbL liposome system, we modulated liposomal core stiffness via liposomal cholesterol content. Drawing from earlier findings that cholesterol increases membrane fluidity within gel-phase liposomes at temperatures below the melting temperature (T_m) of the main phospholipid (22, 23) and that cholesterol added to a stiff, crystalline DSPC liposomal core (T_m ~55 °C) (19, 24) decreases membrane stiffness and increases liposome deformability (21, 25–27), we hypothesized that stiff LbL NPs (S-NPs) formed from "stiff" liposome (S-L) cores (100 mol% 18-carbon saturated phospholipids) and compliant LbL NPs (C-NPs) formed from compliant liposome (C-L) cores (60 mol% 18-carbon saturated phospholipids and 40 mol% cholesterol) would have stiffness-related differences in circulation time, biodistribution, tumor accumulation, and tumor penetration. We elected to keep outer layer composition constant to ensure in vivo performance was based solely on particle stiffness as a function of core cholesterol content. LbL assembly permits us to create LbL NPs with varied core composition and stiffness while maintaining the same outer layer–targeting chemistry (6).

In this study, we demonstrate that the particle stiffness of LbL liposomes can be tuned via cholesterol content. We show that

Significance

Layer-by-layer nanoparticles (LbL NPs), comprised of a charged core substrate layered sequentially with oppositely charged polyelectrolytes, are a promising class of drug delivery carriers for cancer therapeutics with demonstrated success in lowering off-target toxicity and enhancing efficacy. However, little is known about how LbL NP stiffness alters trafficking and delivery. Herein, we report that the stiffness of targeted LbL NPs, comprised of a liposome core and tumor-targeting, polymeric outer layers, can be tuned by altering the mechanical properties of its underlying liposomal core. We also show that these changes have a significant impact on in vivo NP trafficking properties; compliant LbL NPs have longer elimination times, higher organ and tumor accumulation, and higher tumor penetration.

Author contributions: S.M.K. and P.T.H. designed research; S.M.K., D.F.C., and A.J. performed research; S.M.K. contributed new reagents/analytic tools; S.M.K., A.J., K.J.V.V., and P.T.H. analyzed data; and S.M.K., K.J.V.V., and P.T.H. wrote the paper.

The authors declare no competing interest.

This article is a PNAS Direct Submission.

[1]To whom correspondence may be addressed. Email: hammond@mit.edu.

This article contains supporting information online at https://www.pnas.org/lookup/suppl/doi:10.1073/pnas.2104826118/-/DCSupplemental.

following intravenous administration, C-NPs have longer elimination half-lives than S-NPs. We also demonstrate that C-NPs have higher tumor accumulation and a higher degree of particle penetration into subcutaneous tumors, extending prior observations of liposomes (14, 21) to this multicompartment drug delivery system.

Results and Discussion

C-NPs and C-Ls Have Higher Bilayer Fluidity and Lower Effective Elastic Moduli. S-NPs and S-Ls exhibit higher effective elastic moduli. We formulated LbL NPs consisting of an anionic, fluorescently tagged liposome core assembled with two polyelectrolyte layers. S-L cores were formulated with 100 mol% 18-carbon saturated phospholipids (mass ratio 73:20:7 DSPC: DSPG: DSPE), while C-L cores were formulated with 60 mol% 18-carbon saturated phospholipids and 40 mol% cholesterol (mass ratio 48:25:20:7 DSPC:Chol:DSPG:DSPE). Since cholesterol is known to decrease order in fully saturated phospholipid systems (28), and this reduced lipid ordering has been shown to impact elastic modulus (21, 25, 29), bending stiffness (30), and compressibility (31), we hypothesized that cholesterol-containing liposomes (C-L) would be more compliant than 100 mol% fully saturated phospholipid liposomes (S-L) (Fig. 1*A*). DSPC was chosen as the main phase transition lipid for stability since it has a T_m well above that of the human body (T_m = 55 °C). For uniformity, only fully saturated 18-carbon phospholipids were used for additional phospholipid components. DSPG was added to all formulations to ensure a negative liposome charge. DSPE was added for Cyanine7 (Cy7) NHS ester dye conjugation (*SI Appendix*, Table S1). Both liposome cores were then layered with poly-L-arginine (PLR) and terminally layered with hyaluronic acid (HA) via sequential adsorption and purification by tangential flow filtration (TFF) (32). HA is a known ligand of the CD44 receptor up-regulated in ovarian cancer (33, 34), with demonstrated success in targeting nanotherapies (including LbL NPs) to ovarian cancer (6, 35–37).

The effective stiffness of individual NPs was computed as effective elastic moduli E for S-Ls and C-Ls, and S-NPs and C-NPs, using atomic force microscope-enabled indentation on fully hydrated and liquid-immersed NPs. These relative magnitudes differed significantly as a function of NP core composition and not as a function of LbL coating for a given core composition. Specifically, S-Ls and S-NPs exhibited effective E of 21 ± 12 kPa and 24 ± 14 kPa, respectively. In contrast, C-Ls and C-NPs exhibited significantly lower E of 8 ± 3 kPa and 6 ± 3 kPa, respectively. The observation that LbL coating did not significantly impact measured NP stiffness confirms that the elastic properties of LbL NPs are governed most strongly by core composition and demonstrates LbL assembly as a way to modulate NP stiffness while maintaining targeting functionality. Representative force displacement responses are given in Fig. 1*A*, and the measured distribution of elastic moduli ($n = 30$ measurements per composition) are given in *SI Appendix*, Fig. S1, with associated experimental methods. Differences in cholesterol content did not result in significant particle diameter differences in the resulting formulations by dynamic light scattering (DLS) (Fig. 1*B*). S-NPs and C-NPs were 157 ± 3 nm and 167 ± 6 nm in diameter, respectively (100 nm by number average; *SI Appendix*, Fig. S2). Both particles demonstrated similar stability in cell culture media (RPMI + 10% fetal bovine serum [FBS]), HEPES (0 to 200 mM), and NaCl (0 to 100 mM) buffer solutions (*SI Appendix*, Fig. S3).

In order to determine whether cholesterol content alters NP structure, we obtained cryogenic transmission electron microscopy (cryo-TEM) images of our NPs (Fig. 1*C*). These images confirm significant differences in liposomal core structure. S-Ls have a crystalline, faceted appearance. In contrast, C-Ls formulated with cholesterol have a smooth, spherical shape. These observations are consistent with previous studies conducted by Kim et al., in which microparticles formed from fully saturated phospholipids exhibited crystalline domains (24). Given that images were acquired far below the T_m of DSPC (55 °C), at −180 °C, and based on our understanding of cholesterol's role in "fluidizing" the bilayer at temperatures below the T_m (22, 23), the presence of crystalline domains in S-Ls is expected. The domain faceting becomes increasingly pronounced with smaller particles (i.e., NPs), which have a much higher surface curvature than microparticles. S-NPs and C-NPs formulated with S-Ls and C-Ls, respectively, preserve the structures of their liposome cores (Fig. 1*C*). We observed no differences in the layering of S-NPs versus C-NPs (*SI Appendix*, Fig. S4).

C-NPs Have Higher Deformability. Deformability is an important attribute of NPs to characterize as it relates to biodistribution. NPs must pass through discontinuous endothelium in the liver and spleen (200 to 500 nm) in order to return to circulation (10, 38). Based on previous literature demonstrating that more compliant NPs have prolonged blood circulation time (9–13), we hypothesized that a higher proportion of C-NPs would be able to return to circulation because of this relatively higher capacity for deformation. To characterize relative differences in the deformability of our S-NP and C-NP formulations in vitro, we developed an ultracentrifugation spin-down assay. This semiquantitative assay is distinct in that it allows a user to assess relative differences in NP deformability without the use of nanomechanical probes, thus enabling a more rapid and readily available approach to comparing formulations in a relevant, fluid-suspended context under shear flow.

Fluorescently tagged LbL NPs were loaded into the top filter compartment of an ultracentrifugation tube with 200-nm pores. This pore size was selected on the basis that discontinuous endothelial junctions in the spleen are ∼200 to 500 nm wide (10, 39, 40). To be conservative, we chose to conduct this assay with filters having a pore size cutoff at the lower limit of this range. The spleen is a primary filtration organ and has been identified as a key biological barrier-impacting circulation of NPs (9, 10). Under the compressive stresses imparted by centrifugation, we hypothesized that S-NPs and C-NPs would have different levels of NP accumulation within each compartment of the ultracentrifuge tube (retentate, filter, and filtrate). Fluorescence values and DLS derived count rates (DCRs) were used to calculate the proportion of NP in each compartment postspin (Fig. 2*A*). Fluorescence values of the unfiltered sample, retentate, and filtrate demonstrated that C-NPs had a higher degree of NP accumulation in the filter (Fig. 2 *B*, *Left*). This was observed for unlayered liposome cores, PLR single-layer LbL NPs, and PLR/HA bilayer LbL NPs. Unfiltered (not spun), retentate, and filtrate samples were additionally measured for particle concentration using DCR from DLS. NP count results trend with fluorescence results, further confirming the higher accumulation of C-NPs within the filter (Fig. 2 *B*, *Right*). C-NPs additionally had higher accumulation in the filtrate and lower retention in the retentate, suggesting that C-NPs were able to pass through the filter and enter the filtrate more easily (*SI Appendix*, Fig. S5*A*). Prior to measurement, a standard curve-relating DCR to particle concentration was generated at fixed laser attenuation. *SI Appendix*, Fig. S5*B* demonstrates that this relation is linear for the NP concentrations for which this assay was optimized.

To confirm the observed differences in the filter accumulation of S-NPs and C-NPs, a second ultracentrifugation assay was devised (Fig. 2*C*). We hypothesized that NPs caught in the filter would slow the flow of liquid into the filtrate. The extent of filter clogging could be measured by tracking the movement of retentate volume into the filtrate under centrifugation. NP samples were loaded into tubes, spun, and washed to remove residual NP sample from the retentate and filtrate. Ultrapure water was then added to the top of the filter unit, and retentate volume was tracked over time. Tubes that had been previously used to spin-down C-L and C-NPs maintained a larger retentate volume under recentrifugation

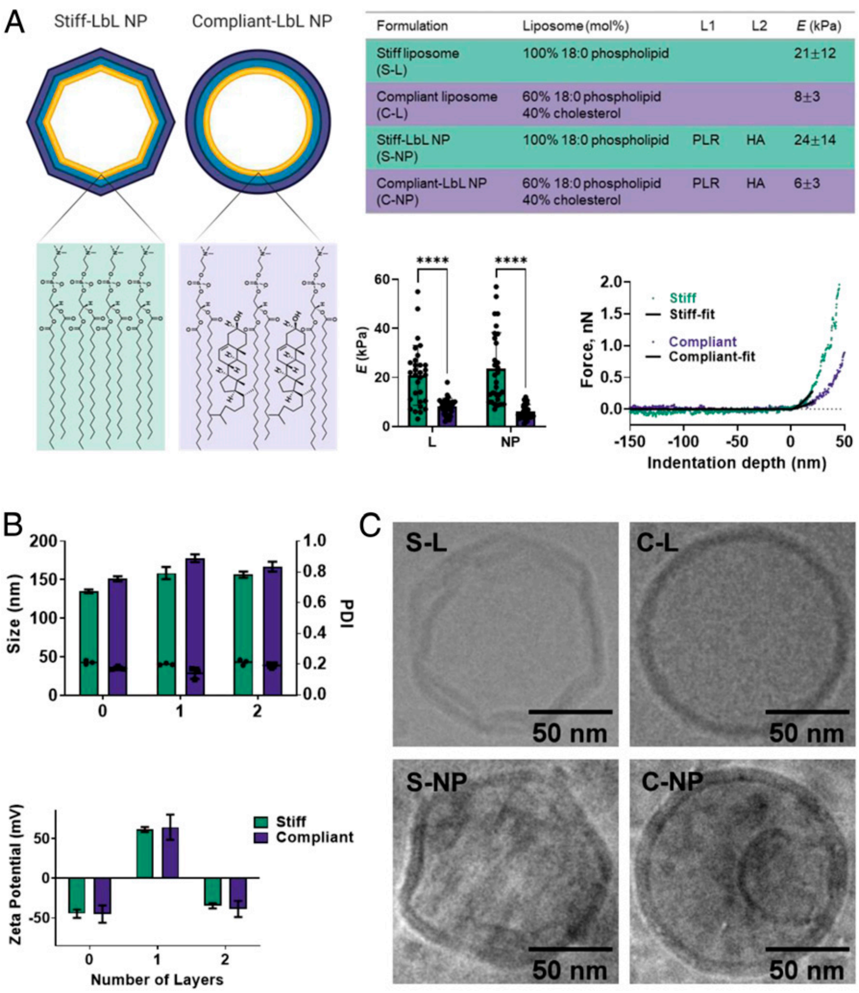

Formulation	Liposome (mol%)	L1	L2	*E* (kPa)
Stiff liposome (S-L)	100% 18:0 phospholipid			21±12
Compliant liposome (C-L)	60% 18:0 phospholipid 40% cholesterol			8±3
Stiff-LbL NP (S-NP)	100% 18:0 phospholipid	PLR	HA	24±14
Compliant-LbL NP (C-NP)	60% 18:0 phospholipid 40% cholesterol	PLR	HA	6±3

Fig. 1. Physicochemical characterization of S-NPs and C-NPs. (*A*) S-Ls and C-Ls are layered with PLR and HA to form S-NPs and C-NPs, respectively. LbL NPs formulated with 18-carbon, fully saturated phospholipids have a high T_m (55 °C). At room temperature, saturated lipid tails pack closely together, forming a stiff structure. In C-NPs, the addition of cholesterol breaks up this tight packing, making liposome more fluid. AFM measurements show that both S-Ls and S-NPs are considerably stiffer than C-Ls and C-NPs (*****P* < 0.0001). No significant difference in effective elastic modulus was detected between liposomes and LbL NPs, confirming that the liposomal core dictates the mechanical properties of the LbL NP. Effective modulus values *E* are reported as mean ± SD. (*B*) S-NPs and C-NPs have similar size and charge by DLS measurements. (*C*) Cryo-TEM images of S-Ls indicate a faceted, crystalline structure. In contrast, C-Ls have a fluid, spherical structure. Postlayering, both S-NPs and C-NPs retain the geometries of the underlying liposomal core.

than S-Ls and S-NPs, indicating a greater extent of filter accumulation for C-NPs (Fig. 2*D*). LbL NPs that passed through the filter and into the filtrate were similar in size and polydispersity index (PDI) to original, unfiltered LbL NPs and experienced a slight reduction in absolute zeta potential (*SI Appendix*, Fig. S5*C*). These ultracentrifugation assays were repeated using 100-nm pore size filter membranes and LbL NPs (*SI Appendix*, Fig. S6). We found that C-NPs had higher filter accumulation and filter clogging than S-NPs. LbL NPs were able to pass from the retentate to the filtrate and experienced a slight decrease in size and increase in zeta potential. Taken together, these data suggest that C-NPs are more deformable, resulting in increased NP–membrane interactions and greater NP accumulation in model membranes. We suggest that higher NP deformability increases contact surface area between NPs and the membrane, resulting in greater frictional forces. These findings are corroborated by atomic force microscopy (AFM) measurements of liposomes; at temperatures below the T_m of the phospholipid, liposomes formulated from fully saturated phospholipids have a higher bending modulus (DPPC system, ∼16×10^{-19} J) than liposomes formulated with a combination of fully saturated phospholipids and cholesterol (50:50 DPPC:cholesterol system, ∼5×10^{-19} J) (25). Others have used physiological, flow-based microcapillary models to demonstrate that more compliant microparticles can squeeze through channels of diameter smaller than a particle's diameter (41).

C-NPs Have a Longer Elimination Half-Life and Higher Splenic and Liver Accumulation in Nontumor-Bearing Mice. Hypothesizing that C-NPs would possess more favorable properties than S-NPs for improving LbL NP circulation half-life, we assessed their in vivo elimination half-life and biodistribution patterns. We chose to use healthy mice in order to examine the direct material impact of the LbL NPs, while mitigating complicating effects due to the disease state.

Mice were treated tail–vein with an injection of either Cy7-tagged S-NPs or C-NPs. Control mice were not injected. Posttreatment, whole-body fluorescence images of the mice were taken with an in vivo imaging system (IVIS) at multiple time points, over a 24-h period. Mice were euthanized at 24 h, and organs were imaged ex vivo for Cy7 LbL NP fluorescence. IVIS time point images were later quantified for whole-body fluorescence values and normalized to mouse body fluorescence immediately postinjection (Fig. 3*A*). C-NPs had a longer elimination half-life ($t_{1/2,\text{fast}} = 1.8$ h and $t_{1/2,\text{slow}} >$ 23 h) compared to S-NPs ($t_{1/2,\text{fast}} = 0.52$ h and $t_{1/2,\text{slow}} = 4.1$ h). Data

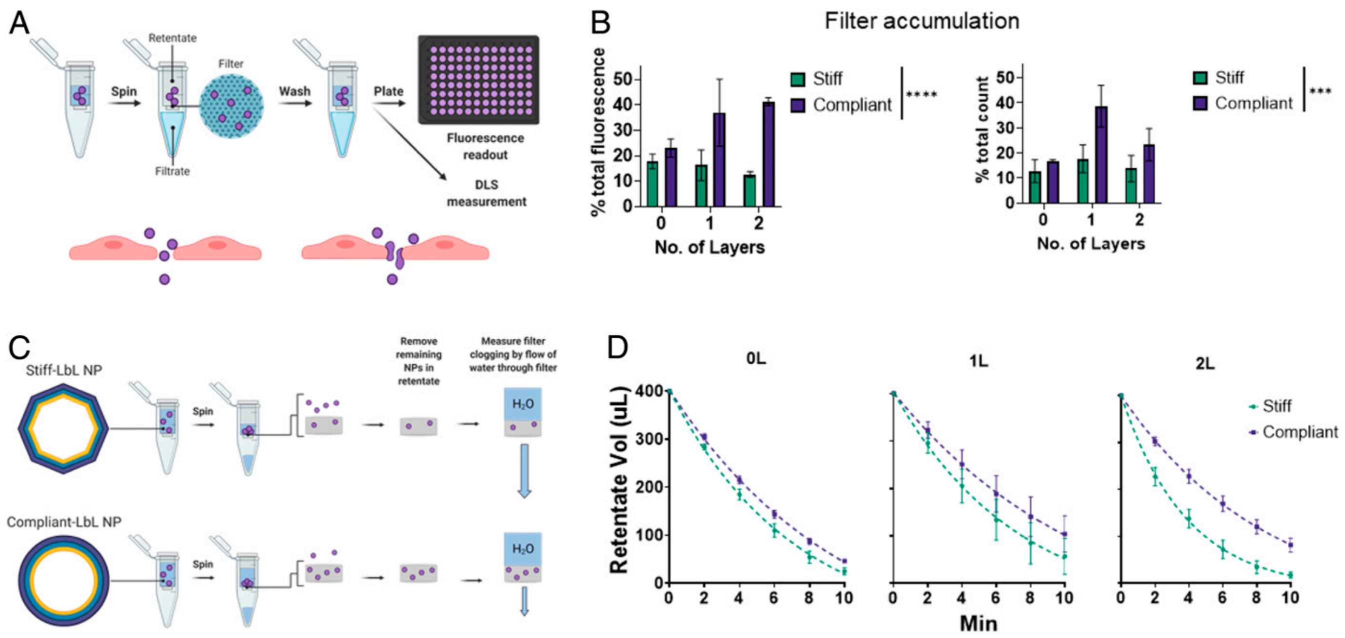

Fig. 2. C-NPs have higher deformability, resulting in increased NP–membrane interactions and greater NP accumulation in model membranes. The filter clogging of compliant materials is a result of higher NP deformability, which increases the contact surface area between membrane and NP, thereby increasing frictional forces at the NP–membrane interface. (*A*) Procedure for ultracentrifugation spin-down assay. Membrane pores (0.2-µm diameter) approximate the discontinuous endothelium found in organs like the liver and spleen, allowing NPs to pass through. NP-loaded ultracentrifuge tubes are loaded and spun. Filtrate and retentate fluorescence and particle count are quantified to determine the proportion of NP accumulation in the filter. (*B*) C-NPs have greater filter accumulation, as quantified by fluorescence signal (****$P < 0.0001$) (*Left*) and NP counts from DLS DCRs (***$P = 0.0003$) (*Right*). (*C*) Procedure for retentate volume assay to probe the degree of filter clogging by S-NPs and C-NPs. Ultracentrifuge tubes containing NP samples are spun, washed to remove NP sample from the filtrate and retentate, and respun with fresh water to determine degree of filter clogging. (*D*) For unlayered (0L), single-layer (1L), and bilayer (2L) NPs, retentate volume is higher for NPs formulated with C-L cores, indicating that C-NPs clog membrane pores to a greater extent, preventing the flow of water from the top of the filter unit.

were fit with a biexponential, two-phase decay model to capture the biphasic nature of NP distribution and elimination post-intravenous bolus administration; this model has been used to describe polyethylene glycol–coated liposomes (42). Area under the curve (AUC) values are 933 ± 69.3 for C-NPs and 582 ± 29.4 for S-NPs, indicating that C-NPs had higher tissue/plasma exposure over time. The finding that C-NPs have longer elimination half-life builds on earlier reports that more compliant particles have longer blood circulation times, owing to their ability to deform and evade biological filtration systems (9–13). This trend has been reported for a wide range of particle sizes (nanometer to micrometer) (9, 11, 43) with or without targeting functionalization (9, 10) and for a wide range of elastic moduli values (kilopascal to gigapascal) (13).

Ex vivo images of Cy7 organ fluorescence indicate that the accumulation of C-NPs was highest in the liver, followed by the kidney and the spleen. In contrast, S-NPs had the highest accumulation in the kidney, followed by the liver and the spleen (Fig. 3 *B–D*). NPs are known to have high accumulation and elimination through the liver and spleen (39), as these are major clearance organs of the mononuclear phagocyte system (MPS). Studies of murine tissues have also shown that the spleen and liver express CD44—a receptor for HA (44). The higher splenic and liver accumulation of C-NPs may be caused by the higher retention of C-NPs in the blood, increasing tissue/plasma exposure to LbL NPs. In addition, studies have reported the increased uptake of stiff NPs by phagocytic cells (9, 45), which may explain the faster clearance of S-NPs over C-NPs. The membrane-wrapping energy required for endocytosis/phagocytosis is reported to be higher compliant NPs (46, 47), resulting in frustrated uptake and the ability of compliant NPs to evade rapid clearance by macrophages and other professional phagocytes.

Elimination half-life and biodistribution data suggest that S-NPs are clearing much more rapidly from blood circulation and accumulating in the kidney. While it is possible that kidney accumulation is caused by dye release, we have found little evidence to support that this is occurring for LbL NPs in this study; in addition to confirming the stability of LbL NPs in media (*SI Appendix*, Fig. S3), we detected <2% free dye in the injected NPs and minimal dye release from LbL NPs over 24 h at physiological conditions (*SI Appendix*, Fig. S7). Dye release studies indicate that a small amount of dye is released upon the initial contact with biological media (within 1 h), but no additional dye release occurs between 1 and 24 h. Given that all dye release occurs within the first hour and renal excretion occurs rapidly for molecules <5 nm (48), significant kidney accumulation from dye release would be expected at time points much earlier than 24 h. Additionally, IVIS images tracking in vivo NP distribution show that, for all LbL NP treatments, particles are concentrated in the liver and not the bladder (*SI Appendix*, Fig. S8). Interestingly, a recent study reported TEM images showing that glycosaminoglycan-functionalized polymeric NPs (130 to 180 nm) can accumulate intact within the kidney via proximal tube secretion, rather than by glomerular filtration (49). Others have reported the significant kidney accumulation of polymeric NPs (50, 51), and several viruses are known to undergo rapid renal excretion despite their large size (155 to 240 nm) (52, 53). Like S-NPs, polymeric NPs and virus particles are stiffer than C-NPs (13, 54), suggesting a link between stiffness and kidney accumulation. However, further studies are required to explore this hypothesis.

C-NPs Have Higher Tumor Accumulation and Longer Elimination Half-Life in Tumor-Bearing Mice. Given that C-NPs possess 1) long elimination half-life (Fig. 3) and 2) enhanced deformability

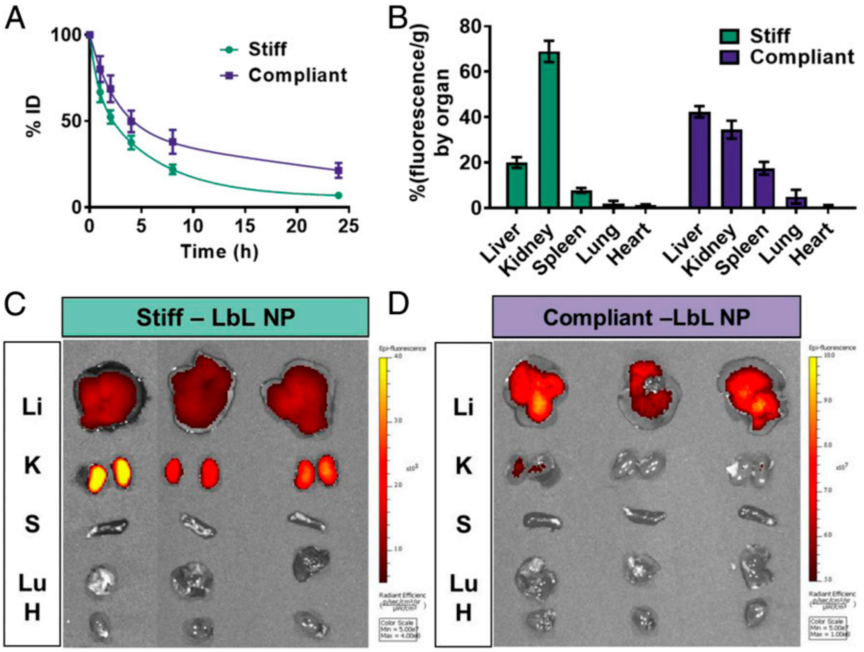

Fig. 3. C-NPs have a longer elimination half-life than S-NPs. S-NPs and C-NPs were administered tail–vein to healthy mice. Mice were imaged over 24 h with IVIS and assessed for organ biodistribution 24-h posttreatment ($n = 3$ per group). (*A*) C-NPs have a longer in vivo elimination half-life ($t_{1/2,\mathrm{fast}} = 1.8$ h and $t_{1/2,\mathrm{slow}} > 23$ h) than S-NPs ($t_{1/2,\mathrm{fast}} = 0.52$ h and $t_{1/2,\mathrm{slow}} = 4.1$ h). (*B*) Particle accumulation was highest in the liver for C-NPs, while it was highest in the kidney for S-NPs, indicating faster elimination of S-NPs. (*C* and *D*) IVIS images of organ biodistribution. Li, liver; K, kidney; S, spleen; Lu, lung; H, heart. For this study only, the Cy7 dye labeling of S-NPs was four times the dye labeling of C-NPs. The color scales in *C* and *D* reflect this. This did not cause appreciable differences in size (S-NP 157 ± 3 nm and C-NP 167 ± 6 nm) or charge (S-NP −37 ± 2 mV and C-NP −48 ± 1 mV).

(Fig. 2), we hypothesized that they could have higher tumor accumulation. Longer elimination half-life increases the chances of passive NP accumulation at the tumor site. We additionally hypothesized that enhanced mechanical fluidity would increase the NP permeation of leaky tumor vasculature. To test this hypothesis, we inoculated mice with subcutaneous OVCAR8 GFP/Luc2-expressing tumors. Luciferized OVCAR8 cells enabled the monitoring of tumor growth and activity via bioluminescence imaging (55). Tumors were allowed to grow for 44 d to an average size of 300 cm^3. Around 1 wk prior to the start of experiments, mice were imaged for bioluminescence activity. Size measurements and bioluminescence values were then used to assign mice to treatment groups with equal tumor burden and tumor activity. Mice were treated tail–vein with formulations of either S-NPs or C-NPs and imaged over 24 h for Cy7 distribution (*SI Appendix*, Fig. S9). Around 24-h postinjection, tumors were imaged ex vivo for Cy7 NP fluorescence and corresponding tumor bioluminescence.

Ex vivo tumor images (Fig. 4*A*) reveal that C-NPs had higher tumor accumulation than S-NPs. Analyzed images indicate that this difference in NP accumulation is significant ($P = 0.0327$). Median NP accumulation for the C-NP group was nearly twice that of the S-NP group (Fig. 4 *B*, *Top*). Tumor activity was similar between treatment groups (Fig. 4 *B*, *Bottom*). C-NPs also had the higher colocalization of Cy7 NP fluorescence with tumor bioluminescence (Pearson's $R = 0.72$) compared to S-NPs (Pearson's $R = 0.38$) (*SI Appendix*, Fig. S10*A*) and a greater degree of overlap between NP signal and tumor bioluminescence signal (*SI Appendix*, Fig. S10 *B* and *C*). Ex vivo images of organs reveal that C-NPs had higher overall particle retention, with large amounts of NP accumulation in the liver (Fig. 4*C*). The comparison of C-NP and S-NP organ fluorescence values reveals that C-NP had higher accumulation in the tumor, spleen, and liver (*SI Appendix*, Fig. S11). As the spleen and liver are major organs of the MPS system, the heightened accumulation of C-NPs in the liver and spleen may be due to longer circulation times. We hypothesize that the increased tumor accumulation of C-NPs results from increased tumor exposure to NPs in the blood, increasing the probability of binding events between targeting moieties on LbL NPs and tumor cells. These data confirm that LbL NP core composition affects material properties that influence tumor accumulation; C-NPs, containing a C-L core, have higher tumor accumulation and higher colocalization with tumor signal.

Similar to our study in healthy mice, C-NPs had a longer elimination half-life than S-NPs (Fig. 4*D*). However, the half-lives of S-NPs and C-NPs were significantly reduced in the tumor-bearing model. We hypothesize that this may be due to an enhanced immune response in tumor-bearing mice, as both NP-treated and untreated tumor-bearing mice display significant splenomegaly (enlargement of the spleen) (*SI Appendix*, Fig. S12 *A* and *B*). The presence of splenomegaly in tumor-bearing mice has been reported (56, 57), and the induction of tumors in mice has been linked to the increasing populations of immune cells in the spleen (58). Additionally, others have reported that the presence of tumors significantly impacts the circulation time of intravenously administered NPs (59, 60). This decrease in circulation time can be dramatic, decreasing NP circulation half-life from 117 min (in healthy mice) to 5 min (in tumor-bearing mice) in one study (60). Tumor induction has been shown to increase macrophage levels and alter circulating secretory factors that influence and increase NP association with M2 macrophage populations in the liver and spleen, as well as monocytes (macrophage precursors) in the blood (59). Interestingly, these trends have been observed in athymic, nude mice. In patients with recurrent epithelial ovarian cancer, the function of circulating monocytes has been linked to the clearance of PEGylated liposomal doxorubicin (61). We hypothesize that an increase in immune cell populations can more quickly clear NPs from circulation. In our study, tumor-bearing mice displayed higher Cy7–NP splenic accumulation than healthy mice, suggesting that NP clearance by immune populations in the spleen could be higher in tumor-bearing mice (*SI Appendix*, Fig. S12*C*). This difference in

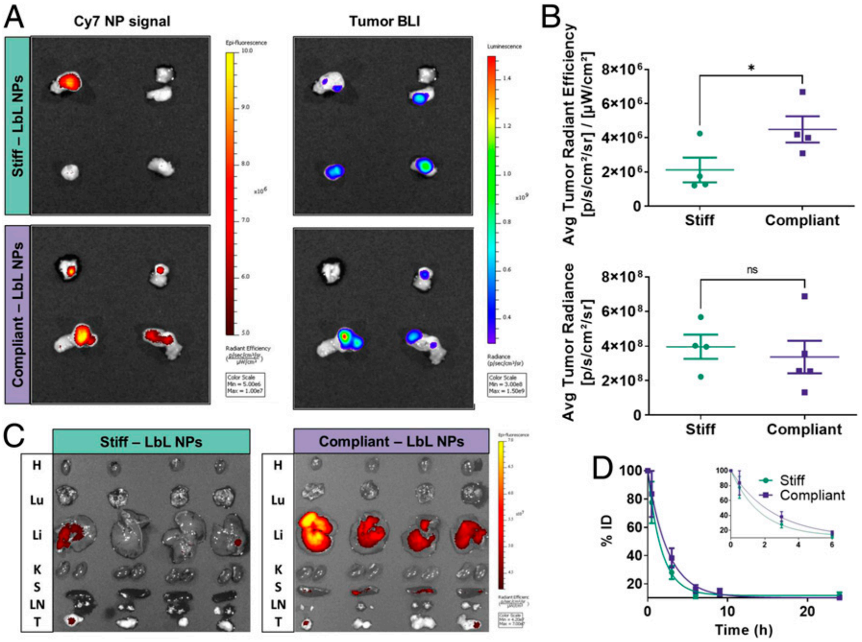

Fig. 4. C-NPs have higher tumor accumulation, higher NP to tumor colocalization, higher particle retention, and longer elimination half-life. Cy7 S-NPs and C-NPs were administered tail–vein to OVCAR8 subcutaneous, tumor-bearing mice. Mice were imaged over 24 h with IVIS and assessed for organ biodistribution 24-h posttreatment (n = 4 per group). (*A*) C-NPs have higher NP–tumor colocalization (Pearson's $R = 0.72$) than S-NPs (Pearson's $R = 0.39$). BLI, bioluminescence image. (*B*) (*Top*) C-NPs have significantly higher tumor accumulation than S-NPs ($*P = 0.03$), indicated by average Cy7–NP fluorescence; (*Bottom*) both treatment groups have similar tumor activity, measured by average bioluminescence radiance. ns, no significance. (*C*) Cy7 NP biodistribution shows the higher particle retention of C-NPs at 24 h. H = heart, Lu = lung, Li = liver, K = kidney, S = spleen, LN = lymph nodes, and T = tumor. Scale is defined for both images. (*D*) C-NPs ($t_{1/2,\text{fast}}$ =1.73 h and $t_{1/2,\text{slow}}$ =1.73 h) have longer elimination half-life than S-NPs ($t_{1/2,\text{fast}}$ = 1.19 h and $t_{1/2,\text{slow}}$ =1.19 h).

immune state may account for the lower levels of NP accumulation in the organs of tumor-bearing mice and slight alterations in biodistribution.

C-NPs Exhibit Higher NP Penetration into Solid Tumors. This study defines NP penetration as the presence of NP signal deep within the solid tumor mass. In order to determine the degree of NP penetration into solid tumors, solid tumors were cryosectioned and imaged for internal NP fluorescence (Cy7) and cell nuclei (DAPI). C-NP–treated tumors had a higher Cy7 signal from tumor cross-sections and thus higher tumor penetration (Fig. 5*A*). For each tumor, multiple regions of interest (ROIs) were measured for NP-integrated density values and tabulated (Fig. 5*B*). Whole images of scanned tumors, as well as representative ROIs, are provided in *SI Appendix*, Fig. S13. Tabulated values indicate that C-NP penetration is higher and statistically significant (P = 0.035). Interestingly, high, surface Cy7 signal did not necessarily correlate with high, internal Cy7 signal for all tumors. Most notably, the only S-NP tumor that appeared to have high-NP accumulation by ex vivo IVIS imaging (Fig. 5 *C*, *Left*; mouse 580) had low-NP signal from the center of the cross-sectioned tumor, suggesting that there was minimal NP penetration into the tumor itself. In tumors treated with S-NPs, an aggregate NP signal lined the periphery of the tumor (*SI Appendix*, Fig. S14). Interestingly, for C-NP–treated tumors, high surface signal from NP accumulation (via ex vivo IVIS imaging) did not necessarily correlate with high-tumor penetration (high-Cy7 NP signal from cross-sections) (Fig. 5 *C*, *Right*).

Within tumors, NPs must navigate an environment of dense stroma and extracellular matrix (62). In vitro studies measuring the diffusion of PEGylated liposomes in poly(ethylene oxide) hydrogels and intestinal mucus have determined that these liposomes exhibit their highest diffusivity at their T_m (19, 20); at 37 °C, PEGylated DSPC liposomes were the most stiff and had lower diffusivity (T_m 55 °C, ∼28 MPa, and 0.478 μm^2/s) than compliant PEGylated DMPC:DPPC liposomes (T_m 36 °C, ∼15 MPa, and 1.689 μm^2/s). Given that cholesterol causes the broadening of the transition temperature, we would expect our C-NPs (containing cholesterol) to have higher penetration and diffusion into the tumor.

In summary, we demonstrated that LbL NPs have tunable stiffness, controlled by the cholesterol content of the liposome core. This difference in stiffness can be significant, with approximately threefold differences impacting an LbL NP's ability to deform and traffic in vivo. Our C-NPs have longer elimination half-life, higher tumor accumulation and higher tumor penetration compared to S-NPs. Our results underscore the importance of NP mechanical properties in targeted delivery systems and suggest that the composition of liposome and liposome-based NP systems influence critical deformation parameters for trafficking to solid tumors. With an LbL NP system, mechanical deformability can be optimized, independent of the exterior outer layer chemistry. Further studies will be required to determine the influence of these material interactions in fully immune–competent systems, in which one can assess the degree to which additional immune cell interactions influence biodistribution and circulation half-life. Additional studies will be needed to determine the local interactions of S-NPs versus C-NPs with tumor and immune cells within solid tumors; this includes how particle stiffness impacts NP internalization and mechanism of uptake, as well as which cells are targeted.

Materials and Methods

Materials and Reagents. The lipids cholesterol, 18:0 PC (1,2-distearoyl-sn-glycero-3-phosphocholine), 18:0 PG (1,2-distearoyl-sn-glycero-3-phospho-(1′-rac-glycerol) (sodium salt), and 18:0 PE (1,2-distearoyl-sn-glycero-3-phosphoethanolamine) were purchased from Avanti Polar Lipids. The polyelectrolytes PLR (38.5 kDa; Alamanda Polymers), HA (20 kDa; LifeCore Biomedical), and dextran sulfate sodium salt (15 kDa; Alamanda Polymers) were used without

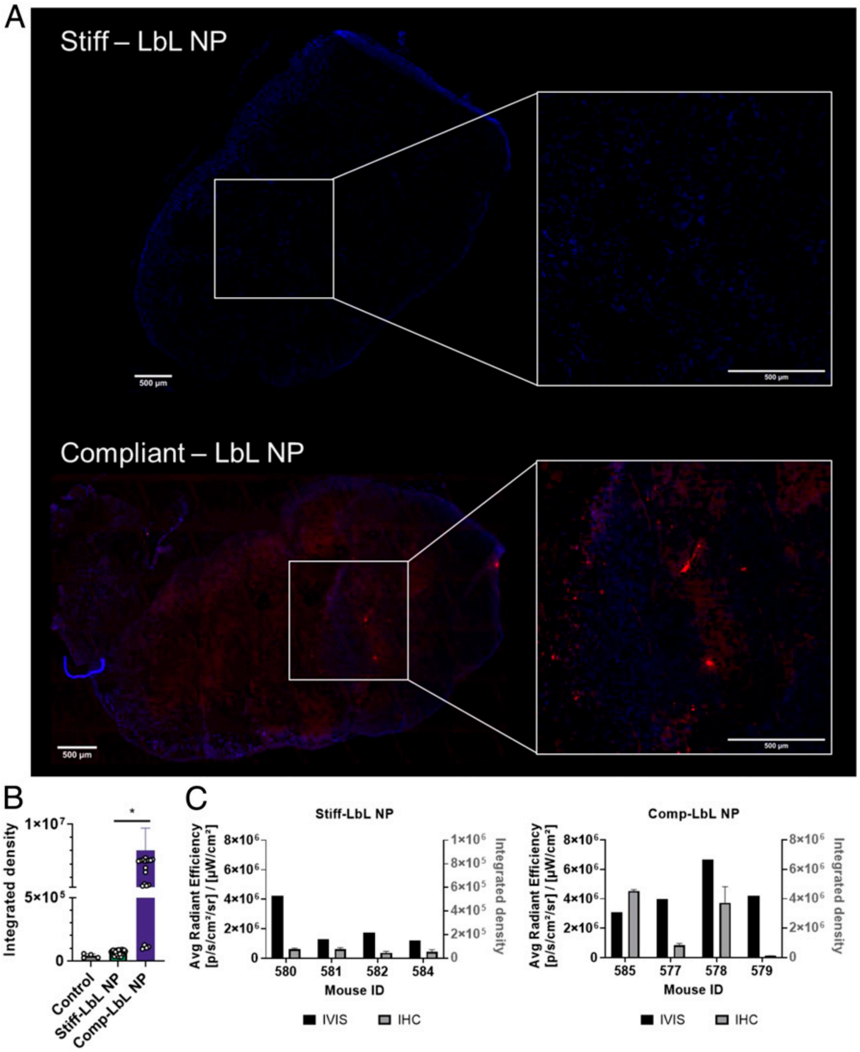

Fig. 5. C-NPs have a higher penetration into solid tumors. Tumors were cryosectioned to compare the Cy7–NP penetration of S-NPs and C-NPs. Cross-sections were imaged for Cy7 fluorescence (NP, red) and DAPI (nuclei, blue). (*A*) Representative regions from the sectioned tumors were captured for each mouse. (*Top*) S-NP-treated tumor. (*Bottom*) C-NP–treated tumor. Reference *SI Appendix*, Fig. 13*A* for whole-tumor images. (*B*) C-NP–treated tumors had higher internal Cy7 signal from cross-sections, indicating higher NP penetration ($^*P = 0.035$). In order to measure the average Cy7 signal from the center of the tumor, ROIs from the center of the tumor were measured for their Cy7-integrated density values. (*C*) For each treatment group, Cy7 average radiant efficiency from IVIS images is plotted along with Cy7 average integrated density values from the cross-sections of the tumor. Note that, although mouse 580 had a higher Cy7 signal from IVIS images, the signal from its tumor cross-sections is low, indicating little tumor penetration of the S-NP formulation. Across most tumors, a high-NP signal from IVIS images did not necessarily correlate with higher penetration. Mouse 585 (C-NP treatment) had the third lowest Cy7 signal from IVIS images but the highest signal from its tumor cross-section. Conversely, mouse 579 had high-Cy7 signal from IVIS but low signal from its tumor cross-section (low penetration). IHC, immunohistochemistry.

modifications. Sulfo-Cy7 NHS ester used for the fluorescent dye conjugation of liposomes was purchased in 5-mg batches from Lumiprobe Inc.

Tissue Culture. OVCAR8 cells were engineered to express GFP/luciferase, as described previously (55). GFP/Luc2 OVCAR8 cells (NCI-60) were cultured in RPMI 1640 (Corning) supplemented with 10% FBS (Gibco) and 1% penicillin streptomycin (Corning) in a Heracell Incubator (Thermo Fisher Scientific) at 37 °C and 5% CO_2. Cells were grown in T175 Corning plasticware coated with poly-L-lysine.

Liposome Formation. Fluorescent liposomes were formed by lipid rehydration, as described previously. Lipids were stored in powdered form and dissolved in chloroform as needed. Mixtures of these lipid solutions were then prepared with and without cholesterol, as described in *SI Appendix*, Table 1. Mixtures were dried until no solvent remained. Solvent evaporation occurred at room temperature, under vacuum, using a BUCHI Rotovap System. Dried lipid films were rehydrated in MilliQ water to a 1 mg/lipid/mL solution under sonication. Lipid solutions were sonicated for 2 min using a Branson sonicator bath filled with MilliQ water at 65 °C. Immediately following sonication, solutions were vortexed for 10 s and allowed to cool to room temperature. Resulting formulations were pushed through a 0.45-µm filter syringe.

Dye Conjugation. The lipid solution was adjusted to pH 8.5, with 200 mM sodium bicarbonate added dropwise into a stirring vial. A total of 5 mg Sulfo-Cy7 NHS ester in powder form was quickly rehydrated into 1-mL 20 mM sodium bicarbonate. The dye solution was added to the stirring lipid solution in a 0.7:2.5 DSPE: sulfo-Cy7 NHS ester mass ratio. Solutions were stirred overnight. Excess dye was removed with 15 washes of the particles using TFF. MilliQ water was used as the exchange buffer. After 15 washes, 0.5 mg/mL fluorescent liposome samples were spun down in 30-K Nanosep Omega Centrifuge Filters to quantify the amount of excess dye remaining in solution. Fluorescence readouts from the filtrate of the centrifuge filter shows that <5% of the liposome fluorescence comes from unconjugated dye.

Layering of Liposomes. Particles were layered by mixing equal volumes of polyelectrolyte and NP solutions under sonication (Branson sonicator bath, room temperature), followed by 10 s of vortexing. This mixture was allowed to rest at room temperature for 15 min, followed by the removal of excess polyelectrolyte from solution using TFF, as described previously (32). A Spectrum Laboratories KrosFlow II system was used to filter the particles. The exchange buffer was MilliQ water. The TFF setup included 100 kDa filter units, purchased from Spectrum C02-E100-05-N, size 13 masterflex Teflon-coated tubing. Samples were filtered at a flow rate of 13 mL/min. Sample filtration was completed after five volume equivalents of permeate were collected. Postfiltration, samples were concentrated by disconnecting the buffer reservoir. The recovery of NPs absorbed onto the filter was achieved by reversing the direction of the peristaltic pump while washing the membrane with pure MilliQ water. The weight equivalents of polyelectrolyte to liposome core are as follows: Layer 1, 0.25 (PLR, 40 kD) and Layer 2, 0.5 (HA, 20 kD).

DLS. NP hydrodynamic size and zeta potential were characterized at each stage of the formulation process using a Malvern ZS90 Particle Analyzer, $\lambda =$ 633 nm, material/dispersant refractive index 1.590/1.330. Samples were measured in 50 uL Sarstedt 67.758 ultraviolet cuvettes (for size measurement) or DTS1070 Malvern-folded capillary tubes (for zeta potential measurement).

TEM. NP images were acquired using a JEOL 2100 field emission gun (FEG) TEM. Frozen samples were prepared in deionized water and acquired by the Koch Institute Nanotechnology Materials Facility. Specifically, 3 μL liposome or the LbL NP sample in DI water was dropped on a lacey copper grid coated with a continuous carbon film and blotted to remove excess sample without damaging the carbon layer by Gatan Cryo Plunge III. The grid was mounted on a Gatan 626 single tilt cryoholder equipped in the TEM column. The specimen and holder tip were cooled by liquid nitrogen. Imaging on the JEOL 2100 FEG microscope was done using minimum dose method to avoid sample damage under the electron beam. The microscope was operated at 200 kV and with a magnification of 10,000 to ∼60,000 for assessing particle size and distribution. All images were recorded on a Gatan 2kx2k UltraScan charge-coupled device camera.

AFM.

Sample prep. NPs were prepared, as described in *Liposome Formation* and *Layering of Liposomes*, and then deposited onto glass slides as a simple substrate to enable the stiffness characterization by mechanical contact. This deposition approach was adapted from a protocol by Takechi-Haraya et al. (25). In brief, fluorescently tagged, anionic liposome solution was deposited onto bovine serum albumin (BSA)-coated glass slides in preparation for force curve collection in liquid. Additional details on the sample prep are provided in *SI Appendix*.

AFM-enabled nanoindentation measurement of NP effective elastic modulus. Force indentation depth data were collected with an atomic force microscope (MFP-3D Bio AFM; Asylum Research) using a silicon cantilever with an attached silicon dioxide spherical indenter probe of 15-μm diameter and a spring constant, k = 0.352 N/m, calibrated via the thermal noise method (63) (NanoandMore, CP-CONT-SiO). A total of 30 independent force depth cycles were collected (each at different sample locations) for each of the four NP sample types (C-Ls, C-NP, S-Ls, and S-NP). The cantilever approach/retraction speed was set to 500 nm/s to avoid particle dispersion, and probe retraction was triggered after reaching the maximum force of ∼6 nN. This response exhibited elastic reversibility for all particle types up to an indentation depth of 20 nm. Thus, effective Young's elastic modulus E was calculated by fitting the Hertz model (64) for an indentation depth of 20 nm, manually confirming the contact point accuracy, and utilizing instrument-integrated analysis for Hertzian contact. We reported distributions (n = 30 per particle type) and mean values of E for each particle type. The statistical comparison of mean E was determined using one-way ANOVA. Note that we express this mechanical attribute as effective mechanical stiffness and effective elastic modulus E with intentional qualification. A detailed discussion on this qualification is provided in *SI Appendix*.

Ultracentrifugation Spin-Down Assay. NP deformability was characterized using an ultracentrifugation assay. Samples were loaded into the top holding unit of the 0.2-μm Nanosep Omega polyethersulfone (PES) ultracentrifuge tubes and centrifuged at prespecified settings. Centrifuge settings (relative centrifugal force, centrifugation time) were optimized prior to data collection and may vary with filter pore size, sample volume, particle concentration, and the inherent mechanical properties of the particle sample. Postcentrifugation, filtrate and retentate samples were assayed for NP fluorescence and DLS DCR. The unfiltered (not spun) sample was used as a reference. To measure filter clogging, fresh MillQ water was added to the top holding unit of the used filters. Ultracentrifuge units were spun at regular intervals, and the mass of the retentate was recorded after each spin in order to track the movement of the retentate volume into the filtrate. Additional experimental details are provided in *SI Appendix*.

In Vivo Biodistribution Studies. Female NCr sp/sp athymic nude mice, 6 wk old, weighing 20 to 30 g (Taconic) were used for all in vivo experiments. Healthy mice were treated intravenously via tail–vein injection with 150 μL Cy7-labeled LbL NPs at a concentration of 0.5 mg/mL (3 mg/lipid/kg body weight) prepared in 5% dextrose (by weight). The NP signal was tracked over 24 h using an IVIS spectrum optical imaging system (PerkinElmer). Elimination half-life data were generated by analyzing fluorescent, whole-body dorsal images of the mice over 24 h using IVIS. Images were analyzed using Living Image software. Background fluorescence was calculated from images of an untreated control mouse and subtracted from the fluorescence values of treatment groups. Final values are represented as a percentage of total administered fluorescent dose postinjection.

After 24 h, mice were euthanized, and their organs were harvested for ex vivo imaging on the IVIS system. Cy7 fluorescent images were taken for all organs and analyzed with Living Image software. Fluorescence values were normalized by organ weight and represented as a percentage of total fluorescence at 24 h. Treatment groups were compared for differences in NP accumulation and tumor bioluminescence via Student's *t* test using GraphPad PRISM software.

In Vivo Tumor Accumulation and Penetration Studies. For tumor studies, ovarian cancer flank models were established via subcutaneous injection of 1×10^6 GFP/Luc2 OVCAR8 cells into the right flank of the mouse (100 μL total volume, mixed 1:1 with Corning matrigel matrix). Tumors were allowed to grow for 44 d, and tumor burden was periodically measured for bioluminescence via IVIS. To measure bioluminescence, 200 μL of 15 mg/mL D-luciferin in Dulbecco's phosphate-buffered saline (DPBS) was injected intraperitoneally into the mice. Images were taken 10 min postinjection, and tumor activity was quantified via luminescence signal using Living Image Software (PerkinElmer). Prior to biodistribution studies, mice were organized to have equal tumor burden across both treatment groups. Mice were treated intravenously via tail–vein injection with 150 uL Cy7-labeled LbL NPs at a concentration of 0.5 mg/mL (3 mg lipid/kg body weight) prepared in 5 wt% dextrose. Elimination half-life data were generated by analyzing fluorescent, whole-body dorsal images of the mice over 24 h using IVIS. Around 24-h posttreatment, Cy7 fluorescent images were taken of all organs.

Ex vivo tumor bioluminescence and Cy7 NP fluorescence images were captured with IVIS. Cy7 fluorescence images were taken prior to bioluminescence. In order to obtain bioluminescence images, tumors were submerged in 2 mg/mL D-luciferin (Thermo Fisher Scientific) for 1 min. Tumors were placed on the imaging mat and imaged 2 min later. A second Cy7 fluorescence image was taken to analyze the colocalization of tumor activity and NP signal.

The colocalization of tumor bioluminescence and Cy7 NP fluorescence was conducted by analyzing bioluminescent and fluorescent IVIS images with ImageJ's Coloc2 plugin to generate a Pearson's R correlation coefficient. Separately, pixel values of bioluminescent and fluorescent images were obtained from ImageJ, and the degree of overlap was calculated as the NP fluorescence signal over tumor bioluminescence signal. Collected pixel values were then plotted in MATLAB to visually recreate the overlay of NP signal (green) on tumor bioluminescence signal (blue).

All animal experiments were approved by the Massachusetts Institute of Technology (MIT) Committee on Animal Care and were conducted under the oversight of the Division of Comparative Medicine.

Immunofluorescence Histology. Following ex vivo IVIS imaging, organ and tumor tissues were embedded in optimal cutting temperature (OCT) compound (Fisher Healthcare Tissue-Plus O.C.T.) and flash frozen over liquid nitrogen in cryomolds (Peel Away Disposable Embedding Mold, Thermo Fisher Scientific). These were maintained at −80 °C before sectioning by the Koch Institute's histology core facility. Slides were cover slipped with hard set–mounting media containing DAPI (H-1800 Vectashield Vibrance Antifade Mounting Medium with DAPI) and allowed to cure at room temperature overnight in the dark. Tissue was left unfixed. Slides were imaged immediately using a Panoramic Slide Scanner P250 (3D Histech). DAPI and Cy7 channels were used to detect nuclei and the NP signal, respectively.

Statistical Analysis. All statistical analysis was performed with GraphPad PRISM 8. Single comparisons were analyzed using a Student's *t* test. For comparing multiple groups, one-way or two-way AVOVA with post hoc Bonferroni analysis was applied.

Data Availability. All study data are included in the article and/or *SI Appendix*.

ACKNOWLEDGMENTS. We would like to acknowledge Apoorv Shanker, Celestine Hong, and Natalie Boehnke for their helpful input in editing this manuscript; Dr. Joelle Straehla for assistance with tail-vein injections; Dr. DongSoo Yun for assistance with taking cryo-TEM images; the Koch Institute Histology core for their help with tumor sectioning; the Bhatia Laboratory for use of their Panoramic Slide Scanner; Dr. Virginia Spanoudaki for her insight and advice on in vivo imaging; the Koch Institute for Integrative Cancer Research at MIT for providing facilities to support this work; the Department of Comparative Medicine at MIT; and we thank the KI Swanson Biotechnology Core. All schematic images were created in BioRender. This work was supported by Department of Defense Ovarian Cancer Research Program Teal Innovator Award OC120504 (to P.T.H.) and the Koch Institute Marble Cancer Research Fund.

1. A. E. Barberio *et al*., Cancer cell coating nanoparticles for optimal tumor-specific cytokine delivery. *ACS Nano* **14**, 11238–11253 (2020).
2. S. Correa *et al*., Tuning nanoparticle interactions with ovarian cancer through layer-by-layer modification of surface chemistry. *ACS Nano* **14**, 2224–2237 (2020).
3. Z. J. Deng *et al*., Layer-by-layer nanoparticles for systemic codelivery of an anticancer drug and siRNA for potential triple-negative breast cancer treatment. *ACS Nano* **7**, 9571–9584 (2013).
4. L. Gu, Z. J. Deng, S. Roy, P. T. Hammond, A combination RNAi-chemotherapy layer-by-layer nanoparticle for systemic targeting of KRAS/P53 with cisplatin to treat non-small cell lung cancer. *Clin. Cancer Res.* **23**, 7312–7323 (2017).
5. S. W. Morton, Z. Poon, P. T. Hammond, The architecture and biological performance of drug-loaded LbL nanoparticles. *Biomaterials* **34**, 5328–5335 (2013).
6. E. C. Dreaden *et al*., Bimodal tumor-targeting from microenvironment responsive hyaluronan layer-by-layer (LbL) nanoparticles. *ACS Nano* **8**, 8374–8382 (2014).
7. E. C. Dreaden *et al*., Tumor-targeted synergistic blockade of MAPK and PI3K from a layer-by-layer nanoparticle. *Clin. Cancer Res.* **21**, 4410–4419 (2015).
8. X. Dang *et al*., Layer-by-layer assembled fluorescent probes in the second near-infrared window for systemic delivery and detection of ovarian cancer. *Proc. Natl. Acad. Sci. U.S.A.* **113**, 5179–5184 (2016).
9. A. C. Anselmo *et al*., Elasticity of nanoparticles influences their blood circulation, phagocytosis, endocytosis, and targeting. *ACS Nano* **9**, 3169–3177 (2015).
10. L. Zhang *et al*., Softer zwitterionic nanogels for longer circulation and lower splenic accumulation. *ACS Nano* **6**, 6681–6686 (2012).
11. T. J. Merkel *et al*., Using mechanobiological mimicry of red blood cells to extend circulation times of hydrogel microparticles. *Proc. Natl. Acad. Sci. U.S.A.* **108**, 586–591 (2011).
12. A. C. Anselmo, S. Mitragotri, Impact of particle elasticity on particle-based drug delivery systems. *Adv. Drug Deliv. Rev.* **108**, 51–67 (2017).
13. Y. Hui *et al*., Role of nanoparticle mechanical properties in cancer drug delivery. *ACS Nano* **13**, 7410–7424 (2019).
14. P. Guo *et al*., Nanoparticle elasticity directs tumor uptake. *Nat. Commun.* **9**, 130 (2018).
15. Q. Liang *et al*., The softness of tumour-cell-derived microparticles regulates their drug-delivery efficiency. *Nat. Biomed. Eng.* **3**, 729–740 (2019). Correction in: *Nat. Biomed. Eng.* **5**, 481 (2021).
16. L. Zhang *et al*., Microfluidic synthesis of hybrid nanoparticles with controlled lipid layers: Understanding flexibility-regulated cell-nanoparticle interaction. *ACS Nano* **9**, 9912–9921 (2015).
17. Y. Hui *et al*., Understanding the effects of nanocapsular mechanical property on passive and active tumor targeting. *ACS Nano* **12**, 2846–2857 (2018).
18. T. Stern *et al*., Rigidity of polymer micelles affects interactions with tumor cells. *J. Control. Release* **257**, 40–50 (2017).
19. M. Yu *et al*., Temperature- and rigidity-mediated rapid transport of lipid nanovesicles in hydrogels. *Proc. Natl. Acad. Sci. U.S.A.* **116**, 5362–5369 (2019).
20. M. Yu *et al*., Rapid transport of deformation-tuned nanoparticles across biological hydrogels and cellular barriers. *Nat. Commun.* **9**, 2607 (2018).
21. H. Wu *et al*., Cholesterol-tuned liposomal membrane rigidity directs tumor penetration and anti-tumor effect. *Acta Pharm. Sin. B* **9**, 858–870 (2019).
22. M. K. Jain, "Role of cholesterol in biomembranes and related systems" in *Current Topics in Membranes and Transport*, F. Bronner, A. Kleinzeller, Eds. (Academic Press, 1975), vol. 6, pp. 1–57.
23. M. Y. el-Sayed, T. A. Guion, M. D. Fayer, Effect of cholesterol on viscoelastic properties of dipalmitoylphosphatidylcholine multibilayers as measured by a laser-induced ultrasonic probe. *Biochemistry* **25**, 4825–4832 (1986).
24. D. H. Kim, M. J. Costello, P. B. Duncan, D. Needham, Mechanical properties and microstructure of polycrystalline phospholipid monolayer shells: Novel solid microparticles. *Langmuir* **19**, 8455–8466 (2003).
25. Y. Takechi-Haraya *et al*., Atomic force microscopic analysis of the effect of lipid composition on liposome membrane rigidity. *Langmuir* **32**, 6074–6082 (2016).
26. R. A. Demel, B. De Kruyff, The function of sterols in membranes. *Biochim. Biophys. Acta* **457**, 109–132 (1976).
27. H. Abumanhal-Masarweh *et al*., Tailoring the lipid composition of nanoparticles modulates their cellular uptake and affects the viability of triple negative breast cancer cells. *J. Control. Release* **307**, 331–341 (2019).
28. J. H. Ipsen, G. Karlström, O. G. Mourtisen, H. Wennerström, M. J. Zuckermann, Phase equilibria in the phosphatidylcholine-cholesterol system. *Biochim. Biophys. Acta* **905**, 162–172 (1987).
29. R. Sorkin, N. Kampf, J. Klein, Effect of cholesterol on the stability and lubrication efficiency of phosphatidylcholine surface layers. *Langmuir* **33**, 7459–7467 (2017).
30. R. S. Gracià, N. Bezlyepkina, R. L. Knorr, R. Lipowsky, R. Dimova, Effect of cholesterol on the rigidity of saturated and unsaturated membranes: Fluctuation and electrodeformation analysis of giant vesicles. *Soft Matter* **6**, 1472–1482 (2010).
31. D. Needham, R. S. Nunn, Elastic deformation and failure of lipid bilayer membranes containing cholesterol. *Biophys. J.* **58**, 997–1009 (1990).
32. S. Correa *et al*., Highly scalable, closed-loop synthesis of drug-loaded, layer-by-layer nanoparticles. *Adv. Funct. Mater.* **26**, 991–1003 (2016).
33. S. Zhang *et al*., Identification and characterization of ovarian cancer-initiating cells from primary human tumors. *Cancer Res.* **68**, 4311–4320 (2008).
34. A. B. Alvero *et al*., Molecular phenotyping of human ovarian cancer stem cells unravels the mechanisms for repair and chemoresistance. *Cell Cycle* **8**, 158–166 (2009).
35. K. Y. Choi *et al*., Smart nanocarrier based on PEGylated hyaluronic acid for cancer therapy. *ACS Nano* **5**, 8591–8599 (2011).
36. S. Ganesh, A. K. Iyer, F. Gattacceca, D. V. Morrissey, M. M. Amiji, In vivo biodistribution of siRNA and cisplatin administered using CD44-targeted hyaluronic acid nanoparticles. *J. Control. Release* **172**, 699–706 (2013).
37. K. Cohen, R. Emmanuel, E. Kisin-Finfer, D. Shabat, D. Peer, Modulation of drug resistance in ovarian adenocarcinoma using chemotherapy entrapped in hyaluronan-grafted nanoparticle clusters. *ACS Nano* **8**, 2183–2195 (2014).
38. R. E. Mebius, G. Kraal, Structure and function of the spleen. *Nat. Rev. Immunol.* **5**, 606–616 (2005).
39. E. Blanco, H. Shen, M. Ferrari, Principles of nanoparticle design for overcoming biological barriers to drug delivery. *Nat. Biotechnol.* **33**, 941–951 (2015).
40. Y. Lu, Z. Gu, Kidney physiology: A size bandpass filter. *Nat. Nanotechnol.* **12**, 1023–1025 (2017).
41. J. Cui *et al*., Super-soft hydrogel particles with tunable elasticity in a microfluidic blood capillary model. *Adv. Mater.* **26**, 7295–7299 (2014).
42. A. Gabizon *et al*., Prolonged circulation time and enhanced accumulation in malignant exudates of doxorubicin encapsulated in polyethylene-glycol coated liposomes. *Cancer Res.* **54**, 987–992 (1994).
43. J. Key *et al*., Soft discoidal polymeric nanoconstructs resist macrophage uptake and enhance vascular targeting in tumors. *ACS Nano* **9**, 11628–11641 (2015).
44. S. J. Kennel, T. K. Lankford, L. J. Foote, S. G. Shinpock, C. Stringer, CD44 expression on murine tissues. *J. Cell Sci.* **104**, 373–382 (1993).
45. Y. Hui *et al*., Nanoparticle elasticity regulates phagocytosis and cancer cell uptake. *Sci. Adv.* **6**, eaaz4316 (2020).
46. X. Yi, H. Gao, Cell membrane wrapping of a spherical thin elastic shell. *Soft Matter* **11**, 1107–1115 (2015).
47. J. Sun *et al*., Tunable rigidity of (polymeric core)-(lipid shell) nanoparticles for regulated cellular uptake. *Adv. Mater.* **27**, 1402–1407 (2015).
48. H. S. Choi *et al*., Renal clearance of quantum dots. *Nat. Biotechnol.* **25**, 1165–1170 (2007).
49. P. P. Wyss *et al*., Renal clearance of polymeric nanoparticles by mimicry of glycan surface of viruses. *Biomaterials* **230**, 119643 (2020).
50. R. M. Williams *et al*., Selective nanoparticle targeting of the renal tubules. *Hypertension* **71**, 87–94 (2018).
51. B. Semete *et al*., In vivo evaluation of the biodistribution and safety of PLGA nanoparticles as drug delivery systems. *Nanomedicine* **6**, 662–671 (2010).
52. R. F. Laine *et al*., Structural analysis of herpes simplex virus by optical super-resolution imaging. *Nat. Commun.* **6**, 5980 (2015).
53. C. Henry, R. J. Hartsock, Z. Kirk, R. Behrer, Detection of viruria in cytomegalovirus-infected infants by electron microscopy. *Am. J. Clin. Pathol.* **69**, 435–439 (1978).
54. I. A. T. Schaap, F. Eghiaian, A. des Georges, C. Veigel, Effect of envelope proteins on the mechanical properties of influenza virus. *J. Biol. Chem.* **287**, 41078–41088 (2012).
55. E. C. Dreaden *et al*., RNA-peptide nanoplexes drug DNA damage pathways in high-grade serous ovarian tumors. *Bioeng. Transl. Med.* **3**, 26–36 (2018).
56. W. D. Mackay, Role of splenomegaly in tumour-bearing mice. *Nature* **205**, 918–919 (1965).
57. W. H. Woglom, The size of the spleen in immune mice. *J. Cancer Res.* **4**, 281–323 (1919).
58. J. E. Markel *et al*., Using the spleen as an *in vivo* systemic immune barometer alongside osteosarcoma disease progression and immunotherapy with α-PD-L1. *Sarcoma* **2018**, 8694397 (2018).
59. M. P. Kai *et al*., Tumor presence induces global immune changes and enhances nanoparticle clearance. *ACS Nano* **10**, 861–870 (2016).
60. R. M. de Kruijff *et al*., Elucidating the influence of tumor presence on the polymersome circulation time in mice. *Pharmaceutics* **11**, 241 (2019).
61. W. P. Caron *et al*., Translational studies of phenotypic probes for the mononuclear phagocyte system and liposomal pharmacology. *J. Pharmacol. Exp. Ther.* **347**, 599–606 (2013).
62. M. W. Dewhirst, T. W. Secomb, Transport of drugs from blood vessels to tumour tissue. *Nat. Rev. Cancer* **17**, 738–750 (2017).
63. J. L. Hutter, J. Bechhoefer, Calibration of atomic-force microscope tips. *Rev. Sci. Instrum.* **64**, 1868–1873 (1993).
64. H. Hertz, On the contact of elastic solids. *Z. Reine Angew. Mathematik* **92**, 156–171 (1881).